nature physics

Article

https://doi.org/10.1038/s41567-025-03134-x

Orbital Seebeck effect induced by chiral phonons

Received: 30 December 2024

Accepted: 11 November 2025

Published online: 21 January 2026

Check for updates

Yoji Nabei[1,2], Cong Yang[2,3], Hong Sun[4], Hana Jones[1,2], Thuc Mai[5], Tian Wang[6], Rikard Bodin[7], Binod Pandey[7], Ziqi Wang[2,3], Yuzan Xiong[8], Andrew H. Comstock[1,2], Benjamin Ewing[1], John Bingen[1], Rui Sun[1,2], Dmitry Smirnov[9], Wei Zhang[8], Axel Hoffmann[10], Rahul Rao[5], Ming Hu[11], Z. Valy Vardeny[7], Binghai Yan[12], Xiaosong Li[6], Jun Zhou[4] ✉, Jun Liu[2,3] ✉ & Dali Sun[1,2] ✉

The orbital angular momentum of electrons presents exciting opportunities for developing energy-efficient, low-power magnetic devices. Typically, the generation of orbital currents is driven by the transfer of orbital angular momentum from 3*d* transition metal magnets, either through the application of an electric field using the orbital Hall effect or through magnetization dynamics. Chiral phonons are quantized lattice vibrations that carry non-zero angular momentum due to the circular motion of atoms. An interplay of chiral phonon dynamics and electrons would enable the direct generation of orbital angular momentum, even without the need for magnetic elements. Here we experimentally demonstrate the generation of orbital currents from chiral phonons activated in the chiral insulator α-quartz under an applied magnetic field and a temperature gradient. We refer to this phenomenon as the orbital Seebeck effect. The generated orbital current is selectively detected in tungsten and titanium films deposited on quartz through the inverse orbital Hall effect. Our findings hold promise for orbitronics based on chiral phonons in non-magnetic insulators and shed light on the fundamental understanding of chiral phonons and their interaction with electron orbitals.

Phonons—quantized lattice vibrations—play crucial roles in determining the thermal, mechanical, optical and electronic properties of crystalline materials. However, their magnetic properties have largely been overlooked, as phonons were traditionally considered linearly polarized, with no angular momentum or magnetic moment. This perspective has recently changed with the discovery of chiral phonons[1,2], which possess finite angular momentum arising from circular or elliptical atomic motion. The observation of chiral phonons occurred at a high-symmetry point in the Brillouin zone of a monolayer of the two-dimensional transition metal dichalcogenide WSe_2 (ref. 2). In addition to these modes at high-symmetry points, chiral phonons have also been observed at locations away from these points in three-dimensional chiral crystals[3–5]. These phonon modes exhibit a finite group velocity, allowing for their propagation by establishing a non-equilibrium phonon distribution in response to a temperature gradient[6,7]. This propagating chiral phonon can interconvert the phonon angular momentum (PAM) into spin angular momentum, as demonstrated by the generation of a spin current in a non-magnetic metal adjacent to a chiral material through the thermal excitation of chiral phonons[8,9]. This phenomenon, analogous to the spin Seebeck effect, has been termed as the chiral-phonon-activated spin Seebeck effect in the presence of large spin–orbit interactions arising from Pb-based chiral materials[8].

A compelling characteristic of chiral phonons is their non-negligible magnetic moment, which may reach the magnitude of the

A full list of affiliations appears at the end of the paper. ✉e-mail: zhoujunzhou@njnu.edu.cn; jliu38@ncsu.edu; dsun4@ncsu.edu

https://doi.org/10.1038/s41567-025-03134-x

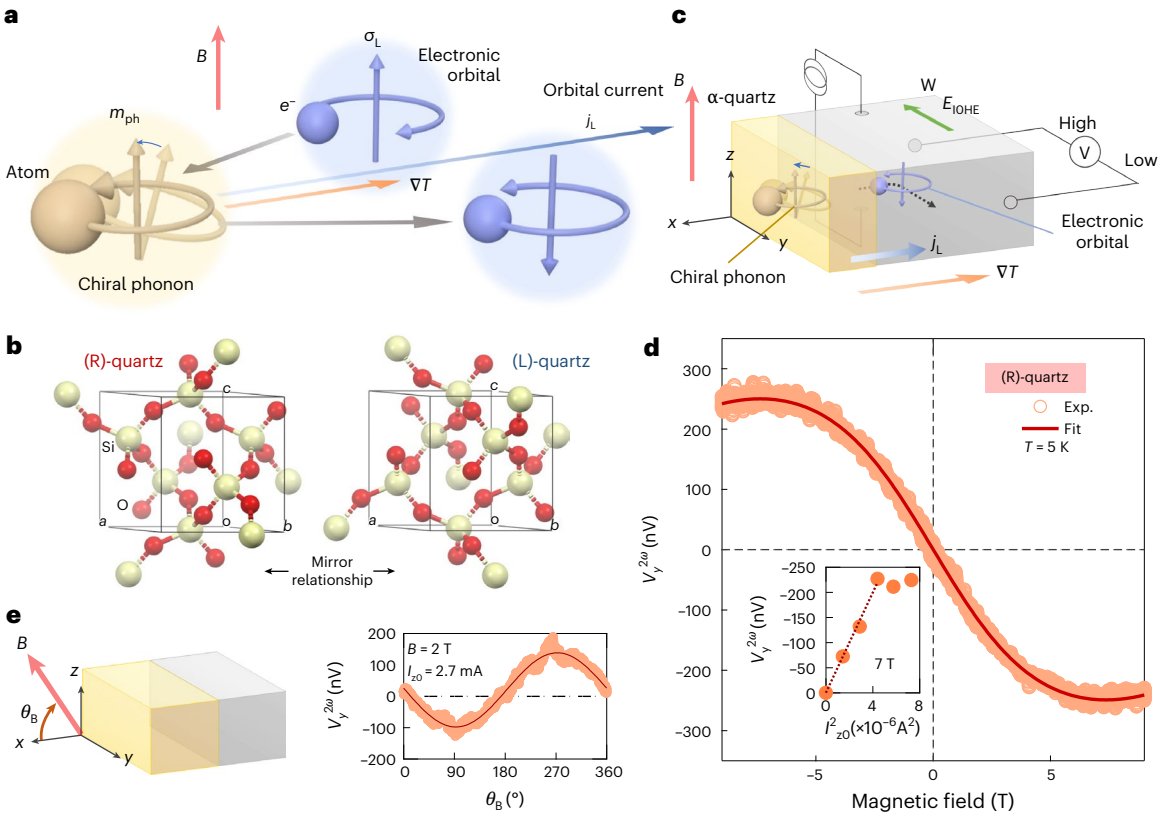

Fig. 1 | Concept and observation of the orbital Seebeck effect originating from chiral phonons. a, Schematic of the orbital Seebeck effect originating from chiral phonons, where PAM polarization is created by the magnetic field **B** (phonon Zeeman effect). When the system is placed in thermal non-equilibrium by applying a temperature gradient **∇T** from the quartz (cold) to NM (hot), the thermal fluctuation is suppressed and the phonon magnetic moment m_{ph} aligns back to the magnetic field direction and transfers its angular momentum into the electronic orbital in NM. As a result, a pure electronic orbital current $\mathbf{j}_L$ is created in the NM. $\boldsymbol{\sigma}_L$ represents the electronic orbital polarization. **b**, Crystal structures of R-quartz and L-quartz. **c**, Schematic of orbital current generation and its detection utilizing IOHE in the present system of the W/(R)-quartz device. $\mathbf{E}_{IOHE}$ represents the electric field induced by IOHE. **d**, Magnetic field (B) dependence of the second-harmonic voltage $V_y^{2\omega}$ for the W/(R)-quartz device. Experimental data are plotted as orange circles. The red line is a fit to the model equation (2). The inset shows the heating power dependence ($\propto I_{z0}^2$) of $V_y^{2\omega}$. **e**, Magnetic field angle (θ_B) dependence of $V_y^{2\omega}$ at $B = 2$ T, with the schematics of the setup. Experimental data are plotted as orange circles. The red line is a sin θ fit with an offset. Data in **d** and **e** were obtained at 5 K by applying an a.c. current $I_{a.c.}$ with amplitude $I_{z0} = 2.7$ mA.

electron Bohr magneton[10–12]. This leads to phonon energy splitting in the presence of an external magnetic field, a phenomenon known as the phonon Zeeman effect[13,14]. The magnetic moment in chiral phonons has been attributed to rich interactions between chiral phonons and the electronic orbitals (Berry curvature). The circular atomic motion in the lattice induces an electronic orbital angular momentum, resulting in the appearance of magnetic moment[15,16]. Such a non-vanishing orbital angular momentum in electrons would be associated with an emerging field known as orbitronics, the orbital counterpart of spintronics. Orbitronics possesses unique advantages over charges and spins for high-performance low-power electronic and magnetic device applications, by enabling orbital angular momentum generation in light elements without relying on spin–orbit interaction[17], and providing low-dissipation transport for information processing[18] and energy-efficient electrical control of magnetic order[19]. Although the generation of orbital angular momentum is typically governed through charge-to-orbital[20,21] and spin-to-orbital[22,23] interconversions in light 3*d* transition metals (for example, Ti and Cr), the emergence of chiral phonon–electronic orbital interaction offers a fascinating possibility of utilizing chiral phonons to produce electronic orbital currents even from insulators in the absence of a charge flow, laying the foundation for energy-efficient orbitronics based on chiral phonons.

Here we report the experimental observation of the chiral-phonon-induced orbital current, demonstrated in a chiral insulator–non-magnetic metal interface, by creating a flow of PAM polarization under the application of an external magnetic field and a temperature gradient, that is, the orbital Seebeck effect (Fig. 1a). The created PAM flow produces the orbital current across the interface, where the orbital current is selectively detected as a voltage drop utilizing the inverse orbital Hall effect (IOHE) in the non-magnetic metal of tungsten (W) and titanium (Ti). Comparing the sign and amplitude of the voltage between W and Ti, we revealed that the orbital current predominantly emerges rather than spin current from a large phonon magnetic moment reaching the Bohr magneton, where the phonon magnetic moment was evaluated within the framework of the Bose–Einstein distribution function. Our findings bridge the fields of chiral phonons and orbitronics, and provide the fundamental understanding of chiral phonons, electronic orbitals and their rich interactions.

Concept and experimental setup

A non-magnetic chiral insulator α-quartz crystal is used for the present study. α-Quartz belongs to a distinguishable chiral trigonal space group $P3_121$ (right-handed, (R)-quartz) or $P3_221$ (left-handed, (L)-quartz). A three-fold screw axis along the *c* axis is achieved by coordinating Si and O atoms, resulting in a helical structure (Fig. 1b). Since chirality guarantees inversion symmetry breaking, α-quartz has chiral phonon modes in reciprocal space[4–6]. We confirmed the existence of chiral phonons in the quartz via circularly polarized Raman spectroscopy[5] (Supplementary Note 1). From the above, the quartz is an ideal experimental platform to investigate the intrinsic magnetic properties of

chiral phonons and orbital current generation in insulators without any magnetic elements.

Figure 1c shows a schematic of our experimental setup to generate and detect the orbital current originating via the phonon Zeeman effect. We prepared a non-magnetic metal (NM) Hall bar contacts on the $(2\bar{1}\bar{1}0)$ surface of the quartz substrate (Methods and Supplementary Note 2). Although quartz possesses chiral phonons with a finite angular momentum, in an equilibrium condition, the net PAM polarization remains zero in the entire system due to time-reversal symmetry[6,7]. Here an external magnetic field is applied to break the time-reversal symmetry, producing the net PAM polarization along the field direction[24]: the magnetic field interacts with chiral phonons, splitting the energy between positively and negatively polarized chiral phonons (phonon Zeeman effect). The net PAM polarization can be injected into the NM by applying a temperature gradient from the quartz (cold) to the NM (hot), where thermal fluctuations in the phonons are suppressed. This suppression allows the phonon magnetic moments to realign with the magnetic field direction (Fig. 1a). As a result, a pure electronic orbital current can be created in the NM by transferring PAM from chiral phonons, where the electrons with an up and down orbital magnetic moment move to the cold and hot sides, respectively. The emerging orbital current can be converted to a transverse charge current via IOHE[17,18,25,26], leading to a voltage along the y direction under open-circuit conditions. W, Ti and platinum (Pt) contacts are selected as the NM layers, since both W and Pt are spin and orbital converters, whereas Ti is merely an orbital converter[27] due to a negligible spin–orbit coupling. It allows us to distinguish the orbital or spin current. Moreover, the NM contact also acts as a local heater: by applying an a.c. current $I_{\mathrm{a.c.}} = I_{z0}\sin\omega t$ along the z direction, a temperature gradient can be established ($\propto I_{z0}^2\sin^2\omega t$) across the NM–α-quartz interface. Therefore, the second-harmonic voltage will correspond to the thermal-related effects and can be probed by a lock-in technique[28] (Methods).

Orbital current generation from the phonon Zeeman effect

Below, we demonstrate the phonon-Zeeman-induced angular momentum current in the W/(R)-quartz device, where the W layer acts as both spin- and orbital-to-charge converter[18,27]. Figure 1d shows the second-harmonic Hall voltage $V_y^{2\omega}$ data measured at temperature $T = 5$ K in the W/(R)-quartz device by applying an a.c. current $I_{\mathrm{a.c.}}$ with amplitude $I_{z0} = 2.7$ mA . The $V_y^{2\omega}$ signal is found to be field dependent: it increases monotonically with increasing magnetic field B and shows saturation and slight decrease at a higher field B > 6 T. The sign of $V_y^{2\omega}$ is inverted by reversing the field direction. We confirm that the observed signal has the typical feature of the voltage induced by heat current; the amplitude of $V_y^{2\omega}$ scales linearly with the current heat power $\propto I_0^2$ (Fig. 1d, inset). Figure 1e shows the magnetic field angle θ_B dependence of $V_y^{2\omega}$ at $B = 2$ T, where B is applied in the x–z plane. The intensity of $V_y^{2\omega}$ varies sinusoidally and shows the maximum value when $\theta_B = 90°, 270°$ ($\mathbf{B} \parallel z$) but vanishes when $\theta_B = 0°, 180°$ ($\mathbf{B} \parallel x$). The absence of $V_y^{2\omega}$ at $\mathbf{B} \parallel x$ is consistent with the anticipated symmetry of IOHE and inverse spin Hall effect (ISHE) response produced via the phonon Zeeman effect. At the $\mathbf{B} \parallel x$ configuration, the PAM polarization points to the x direction, which is parallel to the propagation direction, yielding a null transverse voltage signal because the IOHE (ISHE) voltage is the cross-product of PAM and the propagating vector.

We conducted the B dependence of $V_y^{2\omega}$ in a control sample of a W/glass (amorphous SiO_2) device. Due to its amorphous structure, the glass substrate does not possess any chiral phonons. As shown in Fig. 2a, the $V_y^{2\omega}(B)$ signal is negligibly small, implying that the generated $V_y^{2\omega}$ signal in the W/(R)-quartz device originates from the chiral phonons. Figure 2b shows the B dependence of $V_y^{2\omega}$ in the W/(L)-quartz device. A similar field-dependent $V_y^{2\omega}$ signal also appears in the opposite enantiomer. Remarkably, we found that the sign of the $V_y^{2\omega}$ signal from (L)-quartz was the same as that of (R)-quartz. This result corroborates that the observed signal is induced by the chiral phonons since the PAM polarization should follow the orientation of the applied magnetic field (that is, the phonon Zeeman effect)[13]. It is noteworthy that in the absence of an external magnetic field, the temperature gradient alone can also produce the net PAM polarization in the quartz, the direction of which depends on the structural handedness as revealed by the phonon thermal Edelstein effect[7,9]. Nevertheless, this type of PAM polarization for the point group of the quartz (D_3) is along the x direction (Supplementary Note 3), leading to a zero transverse voltage response because the PAM propagation direction is parallel to the PAM polarization. Thus, we attribute the observed transverse voltage to the phonon Zeeman effect in the present setup.

According to the phonon Zeeman effect, the field dependence of the phonon energy can be described as[13,16]

$$\begin{aligned} E_{l=+1} &= E_0 - \mu_{\mathrm{ph}}B + \sigma_{\mathrm{dia}}B^2, \\ E_{l=0} &= E_0, \\ E_{l=-1} &= E_0 + \mu_{\mathrm{ph}}B + \sigma_{\mathrm{dia}}B^2, \end{aligned} \tag{1}$$

where E_0, μ_{ph} and σ_{dia} represent the phonon energy at $B = 0$, Bohr magneton of the phonon and diamagnetic shift coefficient, respectively. The triple-degenerate phonon modes, of which the angular momentum is $l = +1, 0$ or -1, will split into three energies $E_{l=+1}$, $E_{l=0}$ and $E_{l=-1}$, respectively, by applying a magnetic field. The second and third terms in the equations correspond to the linear and quadratic phonon Zeeman effect. Considering equation (1) and IOHE/ISHE, the $V_y^{2\omega}$ signal in the NM layer can be written as follows:

$$V_y^{2\omega} = A \cdot \frac{\frac{1}{\exp\left(\frac{E_0-\mu_{\mathrm{ph}}B+\sigma_{\mathrm{dia}}B^2}{k_{\mathrm{B}}T}\right)-1} - \frac{1}{\exp\left(\frac{E_0+\mu_{\mathrm{ph}}B+\sigma_{\mathrm{dia}}B^2}{k_{\mathrm{B}}T}\right)-1}}{\frac{1}{\exp\left(\frac{E_0-\mu_{\mathrm{ph}}B+\sigma_{\mathrm{dia}}B^2}{k_{\mathrm{B}}T}\right)-1} + \frac{1}{\exp\left(\frac{E_0}{k_{\mathrm{B}}T}\right)-1} + \frac{1}{\exp\left(\frac{E_0+\mu_{\mathrm{ph}}B+\sigma_{\mathrm{dia}}B^2}{k_{\mathrm{B}}T}\right)-1}}, \tag{2}$$

where, for simplicity, we consider that only the triple-degenerate chiral phonons dominantly contribute to $V_y^{2\omega}$ and these phonons follow the Bose–Einstein distribution. In equation (2), A is a proportionality factor containing the spin/orbital-to-charge conversion coefficient in the NM layers. We found that equation (2) fits well to the observed $V_y^{2\omega}(B)$ curve in the W/(R)-quartz device (Fig. 1d), suggesting that the observed transverse voltage signal is activated by the chiral phonon Zeeman effect. From the obtained fitting parameters, the field-induced phonon energy splitting is derived (Fig. 2c). The degenerated phonon energy located at $E_0 = 0.52$ meV (0.13 THz) splits into the three states $E_{l=+1}$, $E_{l=0}$ and $E_{l=-1}$. At the high field ($B > 6.2$ T), the quadratic phonon Zeeman term plays a more dominant role than the linear term in energy splitting, showing an increase in energy for both states $E_{l=+1}$ and $E_{l=-1}$, which results in the observed voltage saturation and slight decrease at a higher field (Fig. 1d).

Figure 2d shows the temperature dependence of the $V_y^{2\omega}(B)$ plot in the W/(R)-quartz device. The obtained amplitude of the $V_y^{2\omega}$ signal is monotonically enhanced when the temperature decreases (Fig. 2e). This feature is consistent with the signature of the phonon Zeeman effect, where the net PAM polarization of chiral phonons is determined by the population difference between the higher ($E_0 + \mu_{\mathrm{ph}}B + \sigma_{\mathrm{dia}}B^2$) and lower ($E_0 - \mu_{\mathrm{ph}}B + \sigma_{\mathrm{dia}}B^2$) phonon energy state. Since more phonons are distributed in the lower-energy state at a lower temperature, this results in a larger PAM polarization and a larger voltage response. Please note that the recent Kubo formula calculation[29] has revealed that the PAM of chiral phonons does not obey Debye's T^3 law because it is not proportional to the phonon population. We confirmed that the $V_y^{2\omega}(B)$ plots at different temperatures follow the Bose–Einstein distribution model that can be well

https://doi.org/10.1038/s41567-025-03134-x

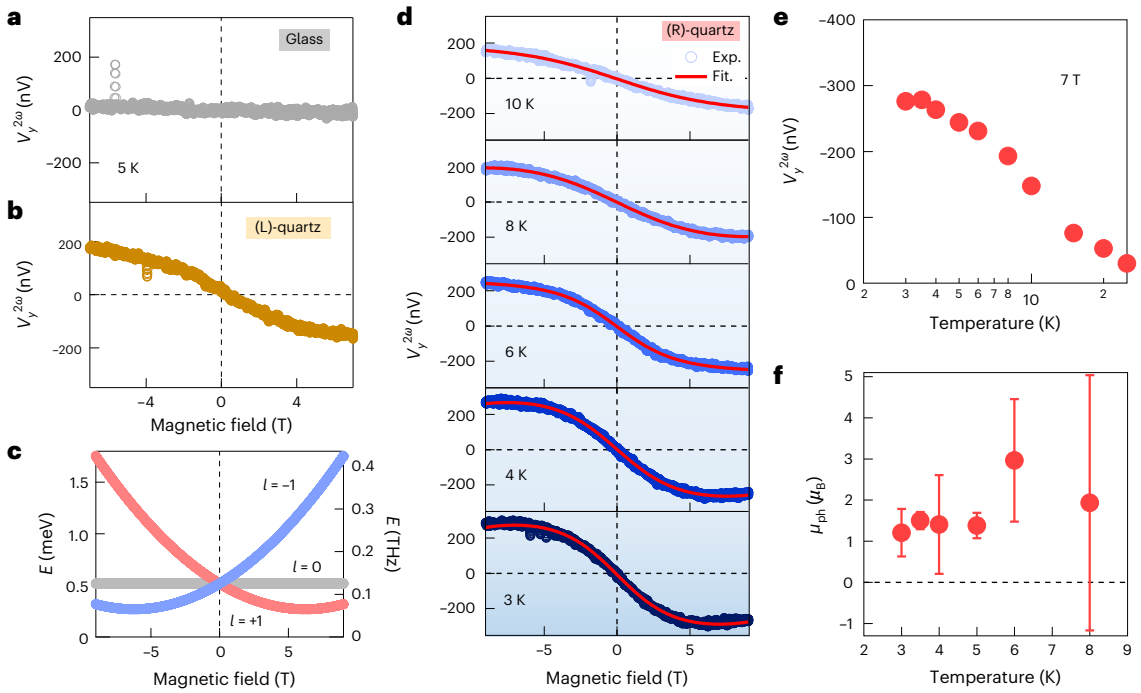

Fig. 2 | Control experiments and temperature dependence. a, B dependence of $V_y^{2\omega}$ for the W/glass (amorphous SiO_2) device. **b**, B dependence of $V_y^{2\omega}$ for the W/(L)-quartz device. The data in **a** and **b** were obtained at 5 K by applying an a.c. current $I_{a.c.}$ with amplitude $I_{z0} = 2.7$ mA. **c**, Visualized field-induced splitting of phonon energy according to the obtained values of fitting parameters. **d**, B dependence of $V_y^{2\omega}$ for the W/(R)-quartz device at the selected temperature by applying an a.c. current $I_{a.c.}$ with amplitude $I_{z0} = 2.7$ mA. Experimental data are plotted by circles. The red line is a fit to the model equation (2). **e**, Temperature dependence of $V_y^{2\omega}$ in the W/(R)-quartz device under a magnetic field $B = 7$ T. **f**, Temperature dependence of the Bohr magneton for the chiral phonon μ_{ph}. The μ_{ph} value was obtained by fitting B dependence of $V_y^{2\omega}$ to equation (2). The error bars in **f** represent one standard deviation of the fitting.

fitted using equation (2). From the fits, the temperature-dependent Bohr magneton of the phonon μ_{ph} is plotted in Fig. 2f (Supplementary Note 4 provides the temperature dependence of E_0, A and σ_{dia}). We found that the obtained μ_{ph} has roughly the same order of magnitude of the electron Bohr magneton μ_B ($\mu_{ph} \approx 1.2\mu_B$). This is three orders of magnitude larger than the expected phonon magnetic moment caused by the motion of ions in the quartz, which is supposed to be equal to the nuclear magneton, $\mu_N \approx 0.5 \times 10^{-3}\mu_B$ (refs. 14,30). The observed large, effective μ_{ph} in the W/(R/L)-quartz would be attributed to the efficient chiral phonon–electron coupling, as discussed in the theories on the phonon Zeeman effect[15]. The circular atomic motion in the chiral phonons induces an electronic orbital response at the NM–α-quartz interface that would represent the amplified phonon magnetic moment.

All our results unambiguously demonstrate that the orbital and/or spin current can be produced in the NM contact by transferring the PAM of chiral phonons lifted by an external magnetic field under the temperature gradient across the NM–α-quartz interface (Supplementary Note 5). Note that the non-reciprocal magnetoresistance[31] including electrical magnetochiral anisotropy[32] does not account for the obtained voltage. In our experimental configuration, the transverse voltage response ($\mathbf{V} \perp \mathbf{I} \parallel \mathbf{B}$) is distinguished from that of the non-reciprocal magnetoresistance ($\mathbf{V} \parallel \mathbf{I}, \mathbf{V} \perp \mathbf{B}$) and electrical magnetochiral anisotropy configuration ($\mathbf{V} \parallel \mathbf{I} \parallel \mathbf{B}$). Moreover, we confirmed that a contribution from the second-harmonic Hall effect[33] was negligible in our measurement (Supplementary Note 6). Spin Seebeck[34], paramagnetic Seebeck[35] and nuclear Seebeck[28] effects can also be ruled out in the present setup because the quartz is non-magnetic and does not have nuclear spin (^{28}Si; 92% natural abundance isotope, nuclear spin $I = 0$, and ^{16}O; 98%, $I = 0$). Consequently, we conclude that orbital and/or spin current created by the chiral phonons solely contribute to the observed voltage.

Orbital versus spin current generation

To identify whether the PAM of chiral phonons is converted into orbital or spin current, below, we investigate the second-harmonic Hall voltage response $V_y^{2\omega}(B)$ in other two NM contacts on top of (R)-quartz substrates: Ti and Pt. W ($Z = 74$) and Pt ($Z = 78$) contacts are both spin- and orbital-to-charge converters with large spin Hall angles of opposite sign[36–38] but have the same sign as the orbital Hall angle[18,27]. By contrast, the Ti contact only acts as an orbital-to-charge converter due to its weak spin–orbit coupling from the lighter element ($Z = 22$)[18,19,27,39]. To systematically compare the $V_y^{2\omega}$ values response in three different devices, the voltage response is normalized as follows. The electric field $\mathbf{E}_{IOHE\,(ISHE)}$ in the NM layer is caused by the IOHE (ISHE) from a cross-product of orbital (spin) current $\mathbf{j}_{L(S)}$ and the orbital (spin)-polarization $\boldsymbol{\sigma}_{L(S)}$ that can be described as[40]

$$\mathbf{E}_{IOHE\,(ISHE)} = (\theta_{OHE\,(SHE)}\rho_{NM})\mathbf{j}_{L(S)} \times \boldsymbol{\sigma}_{L(S)}, \tag{3}$$

where $\theta_{OHE\,(SHE)} = \sigma_{OHE\,(SHE)}/\sigma_{NM}$ is the orbital (spin) Hall angle, $\sigma_{OHE\,(SHE)}$ is the orbital (spin) Hall conductivity, σ_{NM} is the electric conductivity of the NM layer and ρ_{NM} is the electric resistivity of the NM layer. In the present setup, since the orbital (spin) current and its polarization originates from the transferred PAM polarization induced by the phonon Zeeman effect on the temperature gradient, the amplitude of $\mathbf{j}_{L(S)} \times \boldsymbol{\sigma}_{L(S)}$ is proportional to $P_{PAM} \cdot \rho_{NM} j_z^2$, where P_{PAM} is the net PAM polarization and $j_z = j_{z0} \sin \omega t$ is the applied a.c. current density along the z direction. Thus, the detected electric field E_y can be written as $E_y = \gamma_{quartz}\theta_{OHE\,(SHE)}\rho_{NM}^2 P_{PAM} j_{z0}^2 (1 - \cos 2\omega t)/2$, where $\gamma_{quartz} > 0$ is a constant containing the information of the quartz such as heat capacity and thermal conductivity. Therefore, the measured amplitude of the second-harmonic signal $E_y^{2\omega}$ is normalized as $\frac{2E_y^{2\omega}}{\rho_{NM}^2 j_{z0}^2} = -\gamma_{quartz}\theta_{OHE(SHE)}P_{PAM}$. In Fig. 3a–c, $\frac{2E_y^{2\omega}}{\rho_{NM}^2 j_{z0}^2}$ as a function of B is plotted to

https://doi.org/10.1038/s41567-025-03134-x

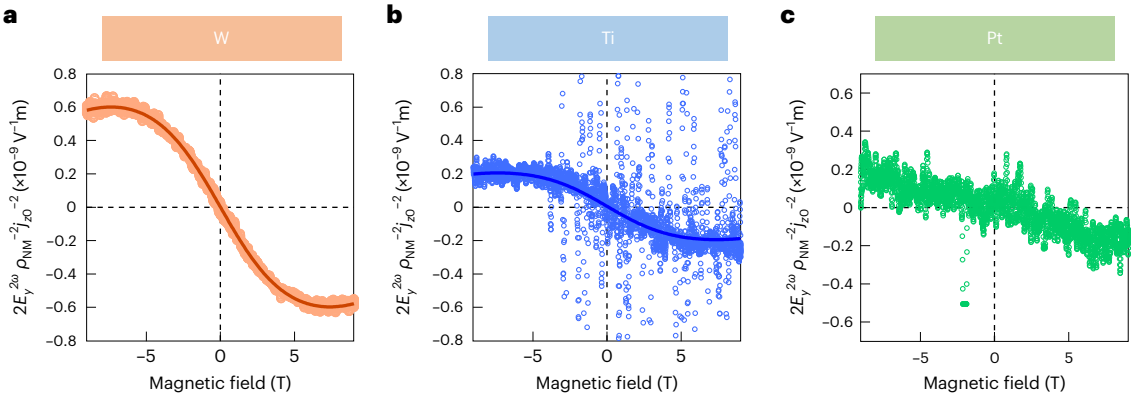

Fig. 3 | Identification of angular momentum current, spin versus orbital. a–**c**, B dependence of the normalized second-harmonic voltage $\frac{2E_y^{2\omega}}{\rho_{NM}^2 j_{z0}^2} = -\gamma_{quartz}\theta_{SHE\,(OHE)}B$ for the W/(R)-quartz (**a**), Ti/(R)-quartz (**b**) and Pt/(R)-quartz (**c**) at 5 K. Experimental data are plotted as circles. The blue line is a fit to equation (2).

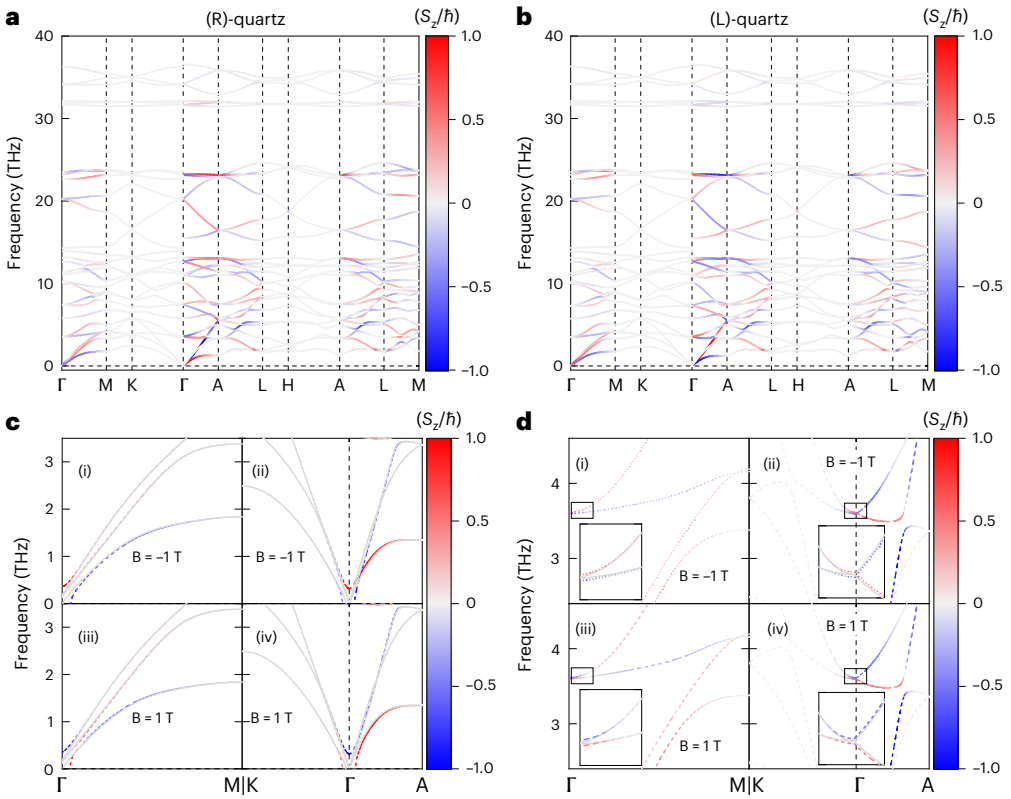

Fig. 4 | Phonons of (R)- and (L)-quartz under different magnetic fields. **a**,**b**, Phonon dispersions of (R)-quartz (**a**) and (L)-quartz (**b**) at $B = 0$ T. **c**,**d**, Variation in acoustic phonons and low-frequency (~4 THz) optical phonons near the Γ point at $B = \pm 1$ T for R-quartz. The solid grey lines and dashed lines represent the absence and presence of magnetic fields, respectively. Here the reduced value ($S_z/\hbar$) of PAM polarization along the z-direction ($s^z_{\mathbf{q}\sigma}$) of phonon mode σ and wave vector **q** is denoted by the colour gradient. Red and blue correspond to positively and negatively polarized phonons.

compare the signals between the W-, Ti- and Pt-based devices. We found that although Ti is the lightest element among the three, the Ti/(R)-quartz device exhibits a measurable B-dependent $V_y^{2\omega}$ signal with a saturation at high fields, which can be well fitted using equation (2) with the same values of E_0, μ_{ph} and σ_{dia} as that in the W/(R)-quartz device. Those are the intrinsic fitting parameters of the chiral quartz regardless of the choice of NM contacts, indicating that these signals are generated by the chiral phonon Zeeman effect. By comparing the amplitude of $V_y^{2\omega}$ signal between the Ti- and W-based devices, the difference in the Hall angle is found to be $\theta^{Ti}_{OHE\,(SHE)}/\theta^{W}_{OHE\,(SHE)} = 0.33$. This ratio is approximately the same as the reported orbital Hall angle ratio 0.29 between Ti and W (ref. 41), whereas it is orders of magnitude different from the previously reported spin Hall angle ratio, namely, 5.1×10^{-4} (refs. 39,42–44). Moreover, we found that the Hall angles for W and Ti are found to be both positive in the present study. This is also consistent with the reported signs of the orbital Hall angles in both metals[18,27,41], in sharp contrast to the reported negative sign of the spin Hall angles[37,39]. Consequently, we concluded that the electronic orbital current is generated by the transferred PAM polarization, that is, the orbital Seebeck effect rather than the spin current generation on the

temperature gradient (Supplementary Notes 7–9 provides further verification of the orbital Seebeck effect).

We note that an earlier study has reported that the chiral phonon creates a spin current at the interface between the chiral quartz and non-magnetic heavy metals[9]. In that case, PAM and spin polarization are produced by the applied temperature gradient along the three-fold screw axis (that is, the phonon thermal Edelstein effect)[7]. That could be distinguished from our present study, where the net PAM polarization of chiral phonons is produced by the magnetic field via the phonon Zeeman effect[10–14]. Since the large phonon Zeeman splitting is related to the electronic orbital contribution[15,16], the chiral phonon-to-orbital conversion plays a dominant role in our setup. Moreover, we treat the chiral phonon modes having linear momentum perpendicular to the PAM ($\mathbf{q} \parallel \boldsymbol{\nabla}\mathbf{T} \parallel \mathbf{x}$; $\mathbf{P}_{\mathrm{PAM}} \parallel z$; Fig. 1c), in sharp contrast to the phonon thermal Edelstein effect in the previous setup[7,9], where the phonons have colinear linear and angular momentum ($\mathbf{P}_{\mathrm{PAM}} \parallel \mathbf{q} \parallel \boldsymbol{\nabla}\mathbf{T} \parallel \mathbf{z}$). This geometrical difference might be related to the selection of orbital and spin current during the transfer process of the angular momentum from the chiral phonons.

It is noteworthy that the Pt/(R)-quartz device shows a linear B-dependent $V_y^{2\omega}$ signal without exhibiting any saturation (Fig. 3c and Supplementary Fig. 10), which cannot be fitted by the phonon Zeeman model function in equation (2) using the same values of E_0, μ_{ph} and $\sigma_{\mathbf{dia}}$ as that in the W/(R)-quartz device. This result implies that the Nernst effect ($\propto \nabla T_x \times B_z$) would dominantly contribute to the obtained voltage signal, instead of IOHE. Moreover, although the predicted orbital Hall conductivity between Pt ($\sigma_{\mathrm{OHE}}^{\mathrm{Pt}}$) and W ($\sigma_{\mathrm{OHE}}^{\mathrm{W}}$) is of the same order[27], the orbital Hall angle of Pt ($\theta_{\mathrm{OHE}} = \sigma_{\mathrm{OHE}}/\sigma_{\mathrm{NM}}$) is roughly one order of magnitude smaller than that of W ($\theta_{\mathrm{OHE}}^{\mathrm{Pt}} \approx \theta_{\mathrm{OHE}}^{\mathrm{W}}/10$) owing to the much higher conductivity in Pt ($\sigma_{\mathrm{NM}}^{\mathrm{Pt}} \approx 10\sigma_{\mathrm{NM}}^{\mathrm{W}}$; ref. 37). This reasonably leads to a negligible IOHE signal in the Pt/(R)-quartz device.

Model and calculations

Combining the results of the first-principles-based density functional theory calculations and the phenomenological theoretical morphic effect[45], we calculated the chiral phonon properties of (R)- and (L)-quartz at different strengths of the magnetic field (Supplementary Note 12). The phonon dispersions of the (R)- and (L)-quartz in the absence of a magnetic field are shown in Fig. 4a,b. The PAM polarization of each phonon mode along the z direction ($s_{\mathbf{q}\sigma}^{z}$) is represented by the colour gradient (red and blue correspond to the positive and negative values, respectively). We confirmed that the negligible difference is in the phonon dispersion between (R)- and (L)-quartz. By possessing opposite structural chirality, the PAM polarization $s_{\mathbf{q}\sigma}^{z}$ are inverted in most acoustic phonon branches, particularly along the high-symmetric path, Γ–A. The calculated chiral phonon properties coincide with previous calculations and experiment reports[4,6,46,47] (Supplementary Note 13).

Since the PAM of each mode is an odd function of the wave vector ($\mathbf{q}$), the total angular momentum is zero under time-reversal symmetry. With the application of an external magnetic field, the time-reversal symmetry is broken, and consequently, a non-zero total PAM is excited as described by the phonon Zeeman effect[24]. As shown in Fig. 4c,d, the phonon branches and PAM in (R)-quartz in the presence of a magnetic field ($B = \pm 1$ T) are calculated. Here we only focus on the low-frequency phonons since all our measurements were performed at low temperatures ($T < 10$ K) and PAM polarization along the z direction. Figure 4c shows the variation in the acoustic phonon modes (0–3 THz) on the magnetic field. The phonon degeneracy in each branch is lifted by the magnetic field and split into two chiral phonons having opposite PAM polarizations. At $B = -1$ T (Fig. 4c(i)), along Γ–M, the acoustic branch with the highest frequency (~0.25 THz at the Γ point) slightly shifts towards a higher frequency, as indicated in equation (1), of which the PAM polarization becomes positively polarized (red colour). By contrast, the lowest-frequency acoustic branch becomes negatively polarized (blue colour). When the magnetic field is reversed, the PAM polarizations from both branches are reversed (Fig. 4c(iii)). We also studied the field-dependent optical branches (~3.5 THz; Fig. 4d). Although a similar splitting of the phonon branch and the generation of PAM polarization are observed, the magnitude of the splitting and PAM polarization are much smaller than those of the acoustic ones, implying that the acoustic phonon branches are responsible for the observed orbital Seebeck effect (Supplementary Note 14).

Outlook

We present the experimental observation of the orbital Seebeck effect in a chiral insulator α-quartz induced by the chiral phonons. We found that a non-zero PAM polarization can be created by the phonon Zeeman effect depending on the orientation of the magnetic field. By applying the temperature gradient across the NM–chiral quartz interface, the PAM from chiral phonons is transferred into the adjacent non-magnetic metallic layer and converted into an electronic orbital current. Moreover, the effective magnetic moment from the chiral phonons reaches one electron Bohr magneton, ~1.2μ_{B}, indicating the great potential of utilizing non-magnetic chiral insulators for constituting energy-efficient orbitronic and caloritronic devices. The observed interconversion of the angular momentum between the chiral phonons and electronic orbitals paves the way for orbitronics utilizing chiral phonons and offers the fundamental understanding of chiral phonon–electronic orbital interactions.

Online content

Any methods, additional references, Nature Portfolio reporting summaries, source data, extended data, supplementary information, acknowledgements, peer review information; details of author contributions and competing interests; and statements of data and code availability are available at https://doi.org/10.1038/s41567-025-03134-x.

References

1. Zhang, L. & Niu, Q. Chiral phonons at high-symmetry points in monolayer hexagonal lattices. *Phys. Rev. Lett.* **115**, 115502 (2015).
2. Zhu, H. et al. Observation of chiral phonons. *Science* **359**, 579–582 (2018).
3. Ishito, K. et al. Truly chiral phonons in α-HgS. *Nat. Phys.* **19**, 35–39 (2022).
4. Ueda, H. et al. Chiral phonons in quartz probed by X-rays. *Nature* **618**, 946–950 (2023).
5. Oishi, E., Fujii, Y. & Koreeda, A. Selective observation of enantiomeric chiral phonons in α-quartz. *Phys. Rev. B* **109**, 104306 (2024).
6. Chen, H. et al. Chiral phonon diode effect in chiral crystals. *Nano Lett.* **22**, 1688–1693 (2022).
7. Hamada, M., Minamitani, E., Hirayama, M. & Murakami, S. Phonon angular momentum induced by the temperature gradient. *Phys. Rev. Lett.* **121**, 175301 (2018).
8. Kim, K. et al. Chiral-phonon-activated spin Seebeck effect. *Nat. Mater.* **22**, 322–328 (2023).
9. Ohe, K. et al. Chirality-induced selectivity of phonon angular momenta in chiral quartz crystals. *Phys. Rev. Lett.* **132**, 056302 (2024).
10. Schaack, G. Magnetic-field dependent phonon states in paramagnetic CeF_3. *Solid State Commun.* **17**, 505–509 (1975).
11. Schaack, G. Observation of circularly polarized phonon states in an external magnetic field. *J. Phys. C: Solid State Phys.* **9**, L297 (1976).
12. Cheng, B. et al. A large effective phonon magnetic moment in a Dirac semimetal. *Nano Lett.* **20**, 5991–5996 (2020).
13. Baydin, A. et al. Magnetic control of soft chiral phonons in PbTe. *Phys. Rev. Lett.* **128**, 075901 (2022).

14. Juraschek, D. M. & Spaldin, N. A. Orbital magnetic moments of phonons. *Phys. Rev. Mater.* **3**, 064405 (2019).
15. Ren, Y., Xiao, C., Saparov, D. & Niu, Q. Phonon magnetic moment from electronic topological magnetization. *Phys. Rev. Lett.* **127**, 186403 (2021).
16. Hernandez, F. G. G. et al. Observation of interplay between phonon chirality and electronic band topology. *Sci. Adv.* **9**, eadj4074 (2023).
17. Jo, D., Go, D., Choi, G.-M. & Lee, H.-W. Spintronics meets orbitronics: emergence of orbital angular momentum in solids. *npj Spintronics* **2**, 19 (2024).
18. Seifert, T. S. et al. Time-domain observation of ballistic orbital-angular-momentum currents with giant relaxation length in tungsten. *Nat. Nanotechnol.* **18**, 1132–1138 (2023).
19. Choi, Y.-G. et al. Observation of the orbital Hall effect in a light metal Ti. *Nature* **619**, 52–56 (2023).
20. Lyalin, I., Alikhah, S., Berritta, M., Oppeneer, P. M. & Kawakami, R. K. Magneto-optical detection of the orbital Hall effect in chromium. *Phys. Rev. Lett.* **131**, 156702 (2023).
21. Rothschild, A. et al. Generation of spin currents by the orbital Hall effect in Cu and Al and their measurement by a Ferris-wheel ferromagnetic resonance technique at the wafer level. *Phys. Rev. B* **106**, 144415 (2022).
22. Xu, Y. et al. Orbitronics: light-induced orbital currents in Ni studied by terahertz emission experiments. *Nat. Commun.* **15**, 2043 (2024).
23. Go, D. et al. Orbital pumping by magnetization dynamics in ferromagnets. *Phys. Rev. B* **111**, L140409 (2025).
24. Komiyama, H. & Murakami, S. Universal features of canonical phonon angular momentum without time-reversal symmetry. *Phys. Rev. B* **103**, 214302 (2021).
25. Hayashi, H., Go, D., Haku, S., Mokrousov, Y. & Ando, K. Observation of orbital pumping. *Nat. Electron.* **7**, 646–652 (2024).
26. Go, D., Jo, D., Lee, H.-W., Kläui, M. & Mokrousov, Y. Orbitronics: orbital currents in solids. *EPL* **135**, 37001 (2021).
27. Salemi, L. & Oppeneer, P. M. First-principles theory of intrinsic spin and orbital Hall and Nernst effects in metallic monoatomic crystals. *Phys. Rev. Mater.* **6**, 095001 (2022).
28. Kikkawa, T. et al. Observation of nuclear-spin Seebeck effect. *Nat. Commun.* **12**, 4356 (2021).
29. Zhong, J. et al. Abnormal phonon angular momentum due to off-diagonal elements in the density matrix induced by a temperature gradient. *Phys. Rev. B* **107**, 125147 (2023).
30. Juraschek, D. M., Fechner, M., Balatsky, A. V. & Spaldin, N. A. Dynamical multiferroicity. *Phys. Rev. Mater.* **1**, 014401 (2017).
31. Ideue, T. et al. Bulk rectification effect in a polar semiconductor. *Nat. Phys.* **13**, 578–583 (2017).
32. Rikken, G. L. J. A., Fölling, J. & Wyder, P. Electrical magnetochiral anisotropy. *Phys. Rev. Lett.* **87**, 236602 (2001).
33. Yokouchi, T., Ikeda, Y., Morimoto, T. & Shiomi, Y. Giant magnetochiral anisotropy in Weyl semimetal WTe_2 induced by diverging Berry curvature. *Phys. Rev. Lett.* **130**, 136301 (2023).
34. Uchida, K. et al. Observation of the spin Seebeck effect. *Nature* **455**, 778–781 (2008).
35. Wu, S. M., Pearson, J. E. & Bhattacharya, A. Paramagnetic spin Seebeck effect. *Phys. Rev. Lett.* **114**, 186602 (2015).
36. Niimi, Y. & Otani, Y. Reciprocal spin Hall effects in conductors with strong spin–orbit coupling: a review. *Rep. Prog. Phys.* **78**, 124501 (2015).
37. Wang, H. L. et al. Scaling of spin Hall angle in 3*d*, 4*d*, and 5*d* metals from $Y_3Fe_5O_{12}$/metal spin pumping. *Phys. Rev. Lett.* **112**, 197201 (2014).
38. Uchida, K. et al. Longitudinal spin Seebeck effect: from fundamentals to applications. *J. Phys. Condens. Matter* **26**, 343202 (2014).
39. Du, C., Wang, H., Yang, F. & Hammel, P. C. Systematic variation of spin-orbit coupling with *d*-orbital filling: large inverse spin Hall effect in 3*d* transition metals. *Phys. Rev. B* **90**, 140407 (2014).
40. Saitoh, E., Ueda, M., Miyajima, H. & Tatara, G. Conversion of spin current into charge current at room temperature: inverse spin-Hall effect. *Appl. Phys. Lett.* **88**, 182509 (2006).
41. Hayashi, H. et al. Observation of long-range orbital transport and giant orbital torque. *Commun. Phys.* **6**, 32 (2023).
42. Pai, C.-F. et al. Spin transfer torque devices utilizing the giant spin Hall effect of tungsten. *Appl. Phys. Lett.* **101**, 122404 (2012).
43. Wang, T.-C., Chen, T.-Y., Wu, C.-T., Yen, H.-W. & Pai, C.-F. Comparative study on spin-orbit torque efficiencies from W/ferromagnetic and W/ferrimagnetic heterostructures. *Phys. Rev. Mater.* **2**, 014403 (2018).
44. Sui, X. et al. Giant enhancement of the intrinsic spin Hall conductivity in beta-tungsten via substitutional doping. *Phys. Rev. B* **96**, 241105 (2017).
45. Anastassakis, E., Burstein, E., Maradudin, A. A. & Minnick, R. Morphic effects—III. Effects of an external magnetic field on the long wavelength optical phonons. *J. Phys. Chem. Solids* **33**, 519–531 (1972).
46. Gonze, X., Charlier, J.-C., Allan, D. C. & Teter, M. P. Interatomic force constants from first principles: the case of α-quartz. *Phys. Rev. B* **50**, 13035–13038 (1994).
47. Strauch, D. & Dorner, B. Lattice dynamics of alpha-quartz. I. Experiment. *J. Phys. Condens. Matter* **5**, 6149 (1993).

[1]Department of Physics, North Carolina State University, Raleigh, NC, USA. [2]Organic and Carbon Electronics Lab (ORaCEL), North Carolina State University, Raleigh, NC, USA. [3]Department of Mechanical and Aerospace Engineering, North Carolina State University, Raleigh, NC, USA. [4]School of Physics and Technology, Nanjing Normal University, Nanjing, China. [5]Air Force Research Laboratory, Dayton, OH, USA. [6]Department of Chemistry, University of Washington, Seattle, WA, USA. [7]Department of Physics and Astronomy, University of Utah, Salt Lake City, UT, USA. [8]Department of Physics and Astronomy, University of North Carolina at Chapel Hill, Chapel Hill, NC, USA. [9]National High Magnetic Field Laboratory, Tallahassee, FL, USA. [10]Department of Materials Science & Engineering and Materials Research Laboratory, The Grainger College of Engineering, University of Illinois at Urbana-Champaign, Urbana, IL, USA. [11]Department of Mechanical Engineering, University of South Carolina, Columbia, SC, USA. [12]Department of Physics, Pennsylvania State University, University Park, PA, USA. ✉e-mail: zhoujunzhou@njnu.edu.cn; jliu38@ncsu.edu; dsun4@ncsu.edu

Methods

Sample preparation

Single-crystal substrates of *x*-cut chiral α-quartz with a size of $12.5 \times 12.5 \times 0.5\ mm^3$ were used, which are commercially available from Precision Micro-Optics. On top of the $(2\bar{1}\bar{1}0)$ plane of chiral α-quartz substrate, W (12 nm), Ti (6 nm) and Pt (12 nm) metal contacts were deposited by radio-frequency magnetron sputtering. The metallic contacts were patterned into a Hall bar configuration using standard photolithography and lift-off methods. The width of the Hall bar is 50 μm and the length between the two voltage probes along with the longitudinal (*z*) direction is 123 μm (Supplementary Fig. 2). To prevent oxidation and degradation, a 4-nm-thick SiO_2 capping layer was deposited on the Ti/chiral quartz device by electron-beam deposition. For the control samples, the same metal Hall bars were fabricated on glass or SiO_2/Si substrates using the same procedure. Note that the SiO_2 layer thermally grown on the Si substrate is amorphous. The measured resistivity of each NM layer is listed in Supplementary Table 1.

Orbital Seebeck effect measurement

The IOHE induced by chiral phonons was measured in a physical property measurement system (Quantum Design). The temperature gradient was created by applying an a.c. current to the metal Hall bar at a frequency of 3 Hz using a current source (6221, Keithley). The produced temperature gradient was confirmed through a transient heat conduction simulation (Supplementary Note 15). The generated Hall voltage responses were recorded using a dual-channel lock-in amplifier (7260, EG&G Instruments). The field-independent second-harmonic offset generated by the capacitive and inductive couplings between the wires to and from the sample was subtracted from the plots, unless otherwise noted. All the second-harmonic voltage $V^{2\omega}$ discussed in the main text are the out-of-phase signal of the lock-in measurement. We confirmed that out-of-phase components were dominant in the second-harmonic signal, as theoretically expected (Supplementary Note 2 and Supplementary Fig. 3).

Calculation method

Phonon dispersion of chiral quartz was calculated using the Vienna ab initio simulation package[48] and the PHONOPY package[49]. The generalized gradient approximation with the PBEsol pseudopotential was adopted for the exchange–correlation function, and the plane-wave energy cut-off was set to be 500 eV. For structure optimization, the energy convergence criterion was set to 10^{-8} eV and ionic relaxations were stopped until Hellmann Feynman forces converge to 10^{-8} eV $Å^{-1}$. The optimized lattice constants are $a = 4.957$ Å and $c = 5.450$ Å. In the harmonic interatomic force constant calculation, a $4 \times 4 \times 4$ supercell was used and only the Γ point was applied. The non-analytical term correction was applied to treat the long-range dipole–dipole interactions. Using the harmonic interatomic force constants, the eigenvector of each phonon mode was solved and the PAM polarizations of all the modes were computed[1] accordingly. A phenomenological theory of morphic effect (developed elsewhere[45]) was used to evaluate the chiral phonons in quartz under magnetic fields.

Data availability

The data that support the findings of this study are available from the corresponding authors upon request. Source data are provided with this paper.

References

48. Kresse, G. & Furthmüller, J. Efficiency of ab-initio total energy calculations for metals and semiconductors using a plane-wave basis set. *Comput. Mater. Sci.* **6**, 15–50 (1996).

49. Togo, A. & Tanaka, I. First principles phonon calculations in materials science. *Scr. Mater.* **108**, 1–5 (2015).

Acknowledgements

D. Sun acknowledges primary financial support from the Department of Energy under award number DE-SC0020992. D. Sun, J.L., X.L. and A.H. acknowledge the Air Force Office of Scientific Research, Multidisciplinary University Research Initiatives (MURI) Program, under award number FA9550-23-1-0311 for the phonon calculation, modelling work and interpretations. Device fabrication at NC State was partially supported by the National Science Foundation (NSF) under award number DMR-2143642. Y.X. and W.Z. acknowledges US NSF under grant number DMR-2509513 for sample preparation assistance. B.Y. acknowledges financial support from the Israel Science Foundation (ISF: 2974/23) and from the Penn State Materials Research Science and Engineering Center for Nanoscale Science from the NSF under award number DMR-2011839. M.H. acknowledges financial support from NSF under grant numbers OAC-2311202 and CNS-2320292. T.M. and R.R. acknowledge funding from Air Force Office of Scientific Research grant number LRIR 23RXCOR003. Z.V.V. acknowledges funding from Air Force Office of Scientific Research grant number 23RT0542 for Raman measurements. The magneto-Raman measurements supported by the US Department of Energy (DE-FG02-07ER46451) were performed at the National High Magnetic Field Laboratory, which is supported by the NSF Cooperative Agreement No. DMR-2128556 and the State of Florida. J.L. acknowledges financial support from the NSF under award number CBET-1943813 for the simulation work done by Z.W.

Author contributions

Y.N., D. Sun, J.L. and J.Z. conceived the experiment and supervised this research. Y.N. was responsible for the magnetotransport measurements. Y.N., W.Z., Y.X., H.J., B.E., J.B. and R.S. fabricated the samples. T.M. and R.R. performed the polarization-dependent Raman measurements. H.S., J.Z., Y.N., X.L., A.H.C., A.H. and B.Y. provided theoretical interpretations. T.W. and X.L. conducted the vibrational circular dichroism calculation. C.Y., H.S. and M.H. conducted the density functional theory calculation and analysis. Z.W. conducted a transient heat conduction simulation under J.L.'s supervision. R.B. and B.P. performed circular-polarization-resolved magneto-Raman spectroscopy under D. Smirnov and Z.V.V's supervision. Y.N. and D. Sun wrote the manuscript. All authors contributed to editing the manuscript.

Competing interests

The authors declare no competing interests.

Additional information

Supplementary information The online version contains supplementary material available at https://doi.org/10.1038/s41567-025-03134-x.

Correspondence and requests for materials should be addressed to Jun Zhou, Jun Liu or Dali Sun.

Peer review information *Nature Physics* thanks Takashi Kikkawa for their contribution to the peer review of this work.